Nanoscale Advances

PAPER

View Article Online
View Journal | View Issue

Cite this: *Nanoscale Adv.*, 2020, **2**, 438

Influence of patch size and chemistry on the catalytic activity of patchy hybrid nonwovens†

Christian Hils,[a] Martin Dulle,[b] Gabriel Sitaru,[c] Stephan Gekle,[c] Judith Schöbel,[d] Andreas Frank,[e] Markus Drechsler,[f] Andreas Greiner[ag] and Holger Schmalz *[ag]

Received 27th September 2019
Accepted 26th November 2019

DOI: 10.1039/c9na00607a

rsc.li/nanoscale-advances

In this work, we provide a detailed study on the influence of patch size and chemistry on the catalytic activity of patchy hybrid nonwovens in the gold nanoparticle (Au NP) catalysed alcoholysis of dimethylphenylsilane in *n*-butanol. The nonwovens were produced by coaxial electrospinning, employing a polystyrene solution as the core and a dispersion of spherical or worm-like patchy micelles with functional, amino group-bearing patches (dimethyl and diisopropyl amino groups as anchor groups for Au NP) as the shell. Subsequent loading by dipping into a dispersion of preformed Au NPs yields the patchy hybrid nonwovens. In terms of NP stabilization, *i.e.*, preventing agglomeration, worm-like micelles with poly(*N*,*N*-dimethylaminoethyl methacrylamide) (PDMA) patches are most efficient. Kinetic studies employing an extended 1st order kinetics model, which includes the observed induction periods, revealed a strong dependence on the accessibility of the Au NPs' surface to the reactants. The accessibility is controlled by the swellability of the functional patches in *n*-butanol, which depends on both patch chemistry and size. As a result, significantly longer induction (t_{ind}) and reaction (t_R) times were observed for the 1st catalysis cycles in comparison to the 10th cycles and nonwovens with more polar PDMA patches show a significantly lower t_R in the 1st catalysis cycle. Thus, the unique patchy surface structure allows tailoring the properties of this *"tea-bag"*-like catalyst system in terms of NP stabilization and catalytic performance, which resulted in a significant reduction of t_R to about 4 h for an optimized system.

Introduction

Noble metal nanoparticles, especially gold nanoparticles (Au NPs), are gaining increasing attention due to their excellent performance in heterogeneous catalysis, ascribed to their extremely high specific surface area.[1–5] For decades, gold has been considered as a poor catalyst since bulk gold is chemically inert. However, when gold is present in the form of small particles with diameters in the nanometer range it becomes surprisingly active.[2,5] First reports on the catalytic activity of Au NPs date back to the 1970s, describing the hydrogenation of alkenes and alkynes with supported Au NPs,[6] followed by the discovery that Au NPs show a high catalytic activity for CO oxidation even at temperatures below 0 °C in 1987.[7] Since then, a plethora of reactions catalysed by Au NPs have been identified, *e.g.* oxophilic activation of epoxides and carbonyl compounds, hydrosilylation reactions, hydrolysis/alcoholysis of silanes, hydrogenation reactions, reduction of aromatic nitro compounds and C–C coupling reactions.[5]

In general, an inherent problem involved in heterogeneous catalysis with NPs is their high specific surface area. On one hand, it is indispensable for a good catalytic performance, but on the other hand it makes the NPs prone to aggregation, which in turn will result in a decreased activity. Thus, efficient strategies have to be developed that can prevent NP agglomeration while preserving their excellent catalytic activity. One common way is the use of low molecular weight or polymeric ligands for NP stabilization. But one has to keep in mind that the ligands can influence the catalytic activity of the NPs as well as the selectivity and the ligands can fade away from the NP surface with time, resulting in

[a]*Macromolecular Chemistry II, University of Bayreuth, Universitätsstraße 30, 95440 Bayreuth, Germany. E-mail: holger.schmalz@unibayreuth.de*
[b]*JCNS-1/ICS-1, Forschungszentrum Jülich GmbH, Wilhelm-Johnen-Straße, 52428 Jülich, Germany*
[c]*Biofluid Simulation and Modeling, Theoretische Physik VI, University of Bayreuth, Universitätsstraße 30, 95440 Bayreuth, Germany*
[d]*Macromolecular Chemistry & New Polymeric Materials, Zernike Institute for Advanced Materials, University of Groningen, Nijenborgh 4, 9747 AG, Groningen, The Netherlands*
[e]*Macromolecular Chemistry I, University of Bayreuth, Universitätsstraße 30, 95440 Bayreuth, Germany*
[f]*Bavarian Polymer Institute, Keylab Optical and Electron Microscopy, University of Bayreuth, Universitätsstraße 30, 95440 Bayreuth, Germany*
[g]*Bavarian Polymer Institute, Keylab Synthesis and Molecular Characterization, University of Bayreuth, Universitätsstraße 30, 95440 Bayreuth, Germany*

† Electronic supplementary information (ESI) available: Characterization of the AuNP dispersion (TEM, DLS, UV-vis, and AF4), the SEDxA triblock terpolymers (^{1}H NMR, FT-IR, μDSC, DLS and TEM), nonwovens based on as-SEDiPA sCCMs and wCCMs (SEM) and details of determination of the Au content in the patchy nonwovens and of treatment of kinetics data. See DOI: 10.1039/c9na00607a

destabilization and, thus, agglomeration.[8,9] Moreover, the complete separation of ligand-stabilized NPs after catalysis is rather difficult, leading to a limited recyclability of the NPs.[10] One strategy to overcome these issues is the immobilization of NPs on a solid inorganic support, like (porous) metal oxides and silica,[11–15] nano-tubes and -rods,[16–18] or two-dimensional layered materials like graphene or graphitic carbon nitride.[19–21] An interesting approach is the use of magnetic iron oxide NPs as a support, facilitating an easy recovery of the catalyst by applying a magnetic field.[22] In addition, metal–organic frameworks (MOFs) have been employed as versatile hosts for metal NPs.[23–25] Besides these examples polymeric supports, like nanocellulose,[26] micro- or nano-porous polymers,[27–31] microgels,[32,33] polyelectrolyte brushes,[34–36] dendrimers and unimolecular micelles,[37,38] as well as polymer micelles,[39–44] are highly attractive for NP stabilization, as their properties can be easily tailored to the demands of a specific catalytic application (NP stabilization, selectivity, and responsivity). In a different approach, polymer nanofibers produced by electrospinning[45,46] or using polyelectrolyte brushes[47] can be used as a sacrificial support for NPs, which can be removed by subsequent calcination. Here, sintering of the NPs occurs during calcination, resulting in porous, mesostructured catalysts that can be easily removed from the reaction media, allowing a good reusability/recyclability. However, due to the sintering of the NPs the catalytically active surface area is partially reduced.

Crystallization-driven self-assembly (CDSA) is increasingly gaining importance for the production of defined cylindrical micelles with tailored functionality for NP stabilization.[48,49] This field was pioneered by the inspiring work of Manners and Winnik on the CDSA of diblock copolymers with a crystallizable poly(ferrocenyl dimethylsilane) (PFS) block. In analogy to living polymerization, CDSA can be conducted in a living manner, using small micellar fragments as seeds for the addition of unimers (molecularly dissolved block copolymers bearing a crystallizable block).[50,51] This seeded-growth protocol paves the way to a precise length control of cylindrical micelles and to a variety of different micellar architectures, like patchy micelles and block comicelles (in analogy to BCPs),[52–55] branched and platelet-like micelles,[56] and hierarchical self-assemblies.[57–59] In addition to PFS-containing BCPs, a variety of other semicrystalline polymers were reported to undergo CDSA, *e.g.* polyethylene (PE),[60,61] poly(L-lactide),[62,63] poly(3-hexylthiophene),[64] oligo(*p*-phenylenevinylene),[65] polycarbonates,[66] or poly(ε-caprolactone).[67]

We have recently shown that Au NP-loaded patchy nonwovens with functional, nanometer-sized patches on the nonwoven's surface are efficient, "*tea-bag*"-like catalyst systems.[68] The patchy nonwovens were prepared by combining coaxial electrospinning[46,69] as a versatile "*top-down*" method with CDSA ("*bottom-up*" approach), employing a polystyrene (PS) solution as the core and a dispersion of functional, patchy worm-like crystalline-core micelles (wCCMs) as the shell (Fig. 1). The patchy wCCMs were produced by CDSA and consist of a semicrystalline polyethylene (PE) core and a corona made of alternating nanometer-sized PS and functional, amino group-containing patches. To this end, the poly(methyl methacrylate) (PMMA)-block of a polystyrene-*block*-polyethylene-*block*-poly(methyl methacrylate) (PS-*b*-PE-*b*-PMMA) triblock terpolymer was functionalized by post-polymerization amidation with *N*,*N*-diisopropylethylenediamine (DiPA) at 130 °C in DMSO.[44] The patchy nonwovens were loaded with catalytically active Au NPs *via* a simple dipping process and showed excellent performance and reusability in the catalytic alcoholysis of dimethylphenylsilane with *n*-butanol. However, due to the comparably harsh conditions used for the amidation of the PS-*b*-PE-*b*-PMMA triblock terpolymer a significant fraction of imide units (amide/imide ≈ 50/50) was formed, leading to a limited solubility of the functionalized triblock terpolymer in THF, the solvent employed for CDSA. Thus, the degree of functionalization of the amidated patches could not be increased above $f \approx 55\%$, as for higher degrees of functionalization the amidated patches were insoluble in THF and CDSA to defined wCCMs was not possible. However, with respect to the efficient stabilization of Au NPs a higher degree of functionalization would be beneficial. In the meantime, we have developed a more efficient amidation method, which will be used in this study. In this approach, the amine is activated with *n*-butyllithium, allowing an almost quantitative amidation without the formation of undesired imide units.[43]

Here, we present a comprehensive study on the influence of micelle geometry as well as patch size and chemistry on the catalytic activity of Au NP-loaded patchy nonwovens, prepared by coaxial electrospinning and subsequent loading with Au NPs *via* a facile dipping process (Fig. 1). Patchy micelles with different shapes (worm-like and spherical), employed as the shell in coaxial electrospinning, were prepared by CDSA of polystyrene-*block*-polyethylene-*block*-poly(*N*,*N*-dialkylaminoethyl methacrylamide) (SEDxA) triblock terpolymers in THF for wCCMs and dioxane for sCCMs (spherical crystalline-core micelles),[60] respectively. The chemistry/polarity of the amidated patches was tuned by using *N*,*N*-diisopropylethylenediamine and *N*,*N*-dimethylethylenediamine for post-polymerization amidation of PS-*b*-PE-*b*-PMMA triblock terpolymers, whereby the size of the patches was altered by using PS-*b*-PE-*b*-PMMA triblock terpolymers with different PS and PMMA weight fractions. The morphology of the neat and Au NP-loaded patchy nonwovens was studied by scanning electron microscopy (SEM) and small-angle X-ray scattering (SAXS). As this study focuses on the influence of the patchy surface structure of the support on the catalytic activity of the embedded Au NPs we have chosen the alcoholysis of dimethylphenylsilane with *n*-butanol as an established model reaction. This allows comparison to our previous results and to literature data.[68,70]

Experimental

Materials

All chemicals were used as received unless otherwise noted. Deionized water (filtered through a Millipore Milli-Q Plus system, QPAK® 2 purification cartridge, conductivity: 18.2 MΩ cm), tetrachloroauric(III) acid trihydrate ($HAuCl_4 \cdot 3H_2O$, 99.99%, Alfa Aesar), sodium borohydride ($NaBH_4$, ≥96%, Fluka), trisodium citrate dihydrate (99% for analytical

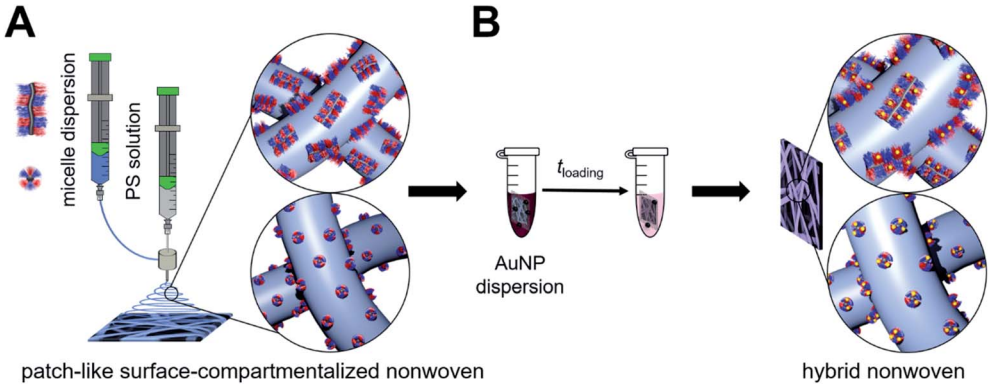

Fig. 1 Preparation of catalytically active hybrid nonwovens: (A) functional, patch-like surface-compartmentalized nonwovens are produced by coaxial electrospinning of PS as the core (grey) and patchy wCCMs or sCCMs as the shell (blue), followed by loading with preformed citrate-stabilized Au NPs by a simple ligand exchange (dipping process (B)).

purposes, Grüssing), dimethylphenylsilane (≥97%, TCI Europe), *n*-butanol (99.9%, anhydrous, Alfa Aesar), undecane (≥99%, Sigma-Aldrich), *n*-butyllithium (2.5 mol L^{-1} in hexane, Acros Organics), *n*-pentane (purified by distillation prior to use), deuterated chloroform ($CDCl_3$, 99.8%, Deutero), calcium hydride (CaH_2, Merck), *N*,*N*-dimethylethylenediamine (DMEDA, ≥98%, Sigma-Aldrich, dried over CaH_2 and purified by distillation), *N*,*N*-diisopropylethylenediamine (DiPEDA, 97%, Acros Organics, dried over CaH_2 and purified by distillation), dry ice, hydrochloric acid (37 wt% in water, VWR), nitric acid (>65 wt% in water, Sigma-Aldrich), ruthenium(III) chloride hydrate (ReagentPlus®, Sigma-Aldrich), sodium hypochlorite solution (NaOCl, 10–15 wt% in water, Sigma-Aldrich), *N*,*N*-dimethylformamide (DMF, 99%, Acros Organics), tetrahydrofuran (THF, ≥99.9%, Sigma-Aldrich, dried by successive distillation over CaH_2 and potassium and stored under nitrogen until use), acetone (99.9%, Acros Organics), dioxane (p.a., AppliChem) and polystyrene (synthesized by anionic polymerization in THF, $M_n = 1.8\ 10^6$ g mol^{-1}, $D = 1.08$). Special care was taken for handling CaH_2, as it strongly reacts with alcohols and water under the formation of hydrogen.

Synthesis of citrate-stabilized Au NPs

The citrate-stabilized Au NPs were prepared according to the procedure reported by Schaal *et al.*[71] To 100 mL of an aqueous $HAuCl_4$ solution ($c = 0.50 \times 10^{-3}$ mol L^{-1}), 9 mL of a $NaBH_4$ solution in water ($c = 4.85 \times 10^{-2}$ mol L^{-1}) were added dropwise followed by stirring for 5 min. The reaction mixture changed colour from yellow to red, indicating the formation of Au NPs. Subsequently, 5 mL of an aqueous sodium citrate solution ($c = 0.05$ mol L^{-1}) were added and the mixture was stirred for another 5 min. Au NPs ($c_{Au} = 0.50 \times 10^{-3}$ mol L^{-1}, determined by inductively coupled plasma-optical emission spectrometry (ICP-OES)) with a mean diameter of $D_{TEM} = 9.5 \pm 2.4$ nm, as determined by transmission electron microscopy (TEM), were obtained (Fig. S1A and B†). The Au NP dispersion showed a localized surface plasmon resonance at $\lambda_{max} =$ 529 nm (Fig. S1C†).

Synthesis of the PS-*b*-PE-*b*-PMMA triblock terpolymers

The PS-*b*-PE-*b*-PMMA triblock terpolymers were synthesized by a combination of living anionic polymerization and catalytic hydrogenation, as published elsewhere.[60] The composition of the employed PS-*b*-PE-*b*-PMMA triblock terpolymers is $S_{40}E_{21}M_{39}^{108}$ and $S_{48}E_{27}M_{25}^{141}$. In this notation, the subscripts describe the mass fraction of the corresponding block in wt% and the superscript denotes the overall number – average molecular weight in kg mol^{-1}. The number-average molecular weight in kg mol^{-1} was determined by a combination of MALDI-ToF MS (matrix-assisted laser desorption/ionization – time of flight mass spectrometry) and ^{1}H NMR (nuclear magnetic resonance) spectroscopy.

Synthesis of SEDxA triblock terpolymers

For the post-polymerization modification of the PS-*b*-PE-*b*-PMMA triblock terpolymers, the PMMA block was amidated with the corresponding *N*,*N*-dialkylethylenediamine (DMEDA, DiPEDA) under an inert argon atmosphere, as published elsewhere.[43] The amidation resulted in quantitative functionalization of the PMMA block, as determined by ^{1}H NMR and FT-IR (Fourier transform-infrared) spectroscopy (Fig. S2 and S3†). The following polystyrene-*block*-polyethylene-*block*-poly(*N*,*N*-dialkylaminoethyl methacrylamide) (SEDxA) triblock terpolymers were prepared: $S_{28}E_{15}DiPA_{58}^{156}$ (s-SEDiPA), $S_{48}E_{21}DiPA_{41}^{181}$ (as-SEDiPA) and $S_{33}E_{17}DMA_{50}^{132}$ (s-SEDMA).

Formation of patchy micelles[60]

The functional, patchy sCCMs of the amidated SEDxA triblock terpolymers were prepared by dissolving the triblock terpolymers in dioxane ($c = 10$ g L^{-1}) at 95 °C for 30 min, followed by cooling to room temperature. The patchy wCCMs were prepared by crystallization-driven self-assembly (CDSA) of the amidated SEDxA triblock terpolymers in THF. To this end, the triblock terpolymers were dissolved in THF ($c = 10$ g L^{-1}) at 65 °C for 30 min and subsequently cooled to the crystallization temperature (T_c, Table S1 and Fig. S4†) of the polyethylene middle block, using a thermostated shaker unit (HLC-MKR 13, Ditabis). The self-assembly process was allowed to proceed for 24 h at a shaking rate of 200 rpm.

Preparation of patchy nonwovens by coaxial electrospinning

For the preparation of patchy nonwovens by coaxial electrospinning, different solutions were prepared. For the core a 7 wt% PS ($M_n = 1.8\ 10^6$ g mol^{-1}) solution in DMF and for the shell dispersions of SEDxA sCCMs or wCCMs in dioxane or THF ($c = 10$ g L^{-1}), respectively, were employed. The fibres were spun on a rotating disk collector (D = 20 cm, 800 rpm) placed at a distance of 5 cm from the coaxial needle (COAX_2DISP sealed coaxial needles, LINARI NanoTech, $d_{core} = 0.51$ mm and $d_{shell} = 1.37$ mm) at a temperature of 20.8 °C and a relative humidity of *ca.* 30%. For electrospinning, a high voltage of 11.4 kV at the needle and −1.0 kV at the collector were applied. The feed rate of the PS core solution was 1.2 mL h^{-1} and for the micellar shell dispersion it was 1.0 mL h^{-1}.

Loading of patchy nonwovens with citrate-stabilized Au NPs (dipping process)

For each system, the loading of the nonwovens was done in an Eppendorf vial by dipping a piece of nonwoven (surface area: S = 1 cm^2 and thickness: $d \approx 400$ μm) fixed in a cage made of a stainless-steel mesh (1.4432 V4A/316L, mesh size: 400 mesh, and wire thickness: 30 μm) into 1 mL of an aqueous, citrate-stabilized Au NP dispersion ($c_{Au} = 0.50 \times 10^{-3}$ mol L^{-1} and $D_{TEM} = 9.5 \pm 2.4$ nm) for 24 h. After incorporation of the Au NPs, the nonwovens were subsequently washed with a sodium citrate solution ($c = 5 \times 10^{-3}$ mol L^{-1}) and water (2 × 5 mL each). The hybrid nonwovens were dried in a vacuum oven (<5 mbar, 40 °C) for 15 h. The amount of Au in the patchy nonwovens was determined by inductively coupled plasma-optical emission spectrometry (ICP-OES, triple determination) and UV-vis measurements (for details see the ESI, eqn (S1) and Fig. S5†) from the respective Au contents of the dispersions before and after loading (difference method).

Catalytic alcoholysis of dimethylphenylsilane

In a typical synthesis, 32 mg of dimethylphenylsilane (0.23 mmol) and 36.7 mg of undecane (0.23 mmol, internal standard for gas chromatography) were dissolved in 4 g of dry *n*-butanol, as published elsewhere.[68] An Au NP-loaded nonwoven (S = 1 cm^2, $d \approx 400$ μm, pre-swollen for 24 h in pure *n*-butanol) was placed in the reaction solution. The reaction was shaken at 400 rpm (Heidolph Multi Reax Shaker) for 24 h and aliquots of 10 μL of the reaction solution were taken after different periods of time for kinetic studies. The aliquots were diluted with 1 mL of acetone for gas chromatography measurements. This procedure was repeated 9 times using the same hybrid nonwoven and a freshly prepared reaction mixture, whereby kinetics were followed for the 1st and 10th cycles only. Before reuse, the Au NP nonwovens were washed with *n*-butanol and dried by placing on a piece of filter paper. The determination of conversion (x_p) *via* gas chromatography was based on the ratio of the integrals of the reactant (dimethylphenylsilane) to the internal standard (undecane, 0.23 mmol) and was referenced to the respective zero measurement.

Instruments

Nuclear magnetic resonance (NMR) spectroscopy. The amidated SEDxA triblock terpolymers were characterized by ^{1}H NMR spectroscopy (Bruker Ultrashield 300 spectrometer) using $CDCl_3$ as solvent. The signal assignment was supported by simulations with NMR software *MestReNova*.

Gas chromatography (GC). The GC measurements were performed on a Shimadzu GC Plus 2010, equipped with an autosampler (AOC 20i) and a Zebron ZB-5ms column (Phenomenex, L = 30 m, ID = 0.25 mm, df = 25 μm, 5% polysilarylene + 95% polydimethylsiloxane; temperature range: 60 to 325/350 °C). The starting temperature was set to 50 °C and kept constant for 2 min. Subsequently, the column was heated to 300 °C at 15 K min^{-1} and kept at 300 °C for 5 min. The overall measurement time was 23 min and nitrogen was used as the carrier gas (purity: 5.0, 1.6 mL h^{-1}). The following retention times (R_t) were observed: R_t(dimethylphenylsilane) = 6.5 min, R_t(undecane) = 8.4 min and R_t(butoxydimethylphenylsilane) = 10.6 min (Fig. S6†).

Asymmetric flow field-flow fractionation (AF4). The AF4 measurement of the AuNP dispersion ($c_{Au} = 0.50 \times 10^{-3}$ mol L^{-1} and $D_{TEM} = 9.5 \pm 2.4$ nm) was performed on an AF2000 Multi Flow Series system from Postnova Analytics, connected to an UV-vis detector (SPD-20A prominence; Postnova Analytics) operated at λ = 530 nm (absorbance maximum of Au NPs (localized surface plasmon resonance, LSPR)) and a DLS detector (Zetasizer Nano-S; Malvern) for signal detection. The flow channel was equipped with a 350 μm spacer and a 10 kDa membrane (regenerated cellulose). Deionized water (Millipore Milli-Q Plus system, QPAK® 2 purification cartridge, conductivity: 18.2 MΩ cm, filtered through a 100 nm membrane) was used as the eluent, employing a detector flow of 0.5 mL min^{-1} and a linear cross flow profile (from 2 mL min^{-1} to 0 mL min^{-1} over 60 min) for separation.

Inductively coupled plasma-optical emission spectrometry (ICP-OES). ICP-OES was performed on a VARIAN Vista-Pro (40 MHz, argon plasma) equipped with an ASX-510 autosampler, echelle polychromator, argon humidifier and ACCD semiconductor detector (calibration to the respective sample matrix with a single gold standard (1000 mg L^{-1}, Merck) and drift correction). The aqueous Au NP dispersions were evaporated at 60 °C, the solid residue was dissolved in 1.5 mL aqua regia, and 0.5 mL of the solution obtained was diluted to 10 mL with deionized water (Millipore Milli-Q Plus system, QPAK® 2 purification cartridge, conductivity: 18.2 MΩ cm). Due to the strong oxidizing and corrosive properties of aqua regia and its decomposition into toxic gases special care has to be taken when handling aqua regia.

Micro-differential scanning calorimetry (μDSC). The measurements were performed on a SETARAM Micro DSC III using sealed measuring cells ("batch cells", V = 1 mL) filled with approx. 0.7 mL of micelle dispersion (c = 10 g L^{-1} in THF). A scan rate of 0.5 K min^{-1} was employed, and pure THF was used as the reference.

Fourier transform-infrared (FT-IR) spectroscopy. The FT-IR spectra were recorded with a Digilab Excalibur 3000 FTIR

instrument equipped with an ATR unit (diamond) at a resolution of 4 cm^{-1}.

Ultraviolet-visible (UV-vis) spectroscopy. The UV-vis measurements were conducted with a JASCO V 630 spectrophotometer (wavelength accuracy: ± 0.7 nm) using a quartz glass cuvette ($D = 10$ mm). A halogen lamp was used as the light source and the sample holder was a JASCO ETCS 761.

Transmission electron microscopy (TEM). The TEM measurements were carried out with a ZEISS/LEO EM922 Omega and a JEOL JEM-2200FS field emission energy filtering transmission electron microscope (FE-EFTEM), both operated at an acceleration voltage of 200 kV. Zero-loss filtered micrographs ($\Delta E \approx 0$ eV) were recorded with a CCD camera system (Ultrascan 1000, Gatan) in the case of the ZEISS Omega and a bottom mounted CMOS camera system (OneView, Gatan) for the JEOL JEM-2200FS, respectively. The images were processed with digital image processing software (DM 1.9 and DM 3.3, Gatan). For TEM analysis of the triblock terpolymer micelle dispersions (wCCMs and sCCMs), the samples were diluted to a concentration of $c = 0.1$ g L^{-1} and stirred for 30 min at room temperature. Subsequently, 10 μL of the respective dispersion was applied to a carbon-coated copper grid and residual solvent was removed by blotting with a filter paper followed by drying of the coated copper grid in a vacuum oven (24 h, 2 mbar, and room temperature). For selective staining of PS, the samples were treated for 11 min with RuO_4 vapor, which was formed *in situ* from $RuCl_3$ hydrate and NaOCl. After staining, the samples were stored for at least 1 h in a fume hood to ensure that any not reacted RuO_4 was completely removed. The average wCCM lengths and patch sizes of the triblock terpolymer micelles as well as the average size of the Au NPs were determined by measuring at least 100 micelles/NPs using *ImageJ* software (Fig. S7†).[72]

Scanning electron microscopy (SEM). The SEM measurements on samples sputter coated with platinum were performed on a Zeiss 1530 with a field emission cathode at an acceleration voltage of 1–10 kV (detectors: back scattered electron (BSE), secondary electrons (SE2) and Inlens SE). The samples were applied to a conductive adhesive carrier mounted on an aluminium plate, fixed with an aluminium adhesive strip and coated with a thin platinum layer ($d \approx 1.3$ nm, Cressington 208HR high resolution sputter coater with an MTM-20 thickness controller). The average diameter of the fibres was determined by measuring at least 100 fibres using *ImageJ* software.[72]

For SEM measurements on the uncoated patchy nonwovens based on s-SEDiPA wCCMs (NW_s-SEDiPA(w)) a FEI Quanta FEG 250 scanning electron microscope (Thermo Fisher Scientific) equipped with a field emission gun was used. The measurements were conducted under high vacuum at an acceleration voltage of 6 kV by utilizing the beam deceleration mode. This mode is used in this case to image surfaces at high magnification with a back scattered electron detector, which is insensitive to sample charging. Here, an additional negative voltage (bias, −4 kV) was applied to the stage and, thus, to the sample. The primary electrons are decelerated to 2 kV when reaching the sample and the signal electrons are accelerated toward the centric back scattering electron detector.

Small angle X-ray scattering (SAXS). The scattering patterns were recorded with a SAXS system "Ganesha-Air" from (SAXSLAB/XENOCS). The X-ray source of this laboratory based system is a D2-MetalJet (Excillum) with a liquid metal anode operating at 70 kV and 3.57 mA with Ga-K_α radiation (wavelength $\lambda = 0.13414$ nm), providing a very brilliant and a very small beam (<100 μm). The beam was slightly focused with a focal length of 55 cm, using a specially made X-ray optics (Xenocs) to provide a very small and intense beam at the sample position. Two pairs of scatterless slits were used to adjust the beam size depending on the detector distance. The data were acquired with a position-sensitive detector (PILATUS 300K, Dectris). Different detector positions were used to cover the range of scattering vectors between 0.04 and 5.0 nm^{-1}. The measurements were performed at room temperature in 1 mm glass capillaries (Hilgenberg, code 4007610, Germany) or directly on the nonwovens. The circularly averaged data were normalized to the incident beam, sample thickness and measurement time before subtracting the background, which was water for the NP dispersion and the neat (unloaded) patchy nonwoven for the hybrid nonwovens, respectively.

Dynamic light scattering (DLS). DLS measurements were performed on an ALV DLS/SLS-SP 5022F compact goniometer system with an ALV 5000/E cross-correlator at a scattering angle of $\theta = 90°$ and 23 °C, using a HeNe laser (max. 35 mW, $\lambda = 632.8$ nm) as the light source. The time-dependent scattering intensity was monitored with an APD (avalanche photodiode)-based pseudo cross correlation system. All samples were filtered through 0.45 μm PTFE syringe filters (BGB Analytik) and filled into NMR tubes (VWR, 5 mm outer diameter) for measurement. For each sample at least 3 measurements were averaged. The

Table 1 Characteristics of the employed SEDxA triblock terpolymers and micellar dispersions

Sample code	Composition[a]	Block length PS/PDxA	PDxA corona [wt%]	R_h (sCCMs)[b] [nm]	l (wCCMs)[c] [nm]	Patch size PS/PDxA[c] [nm]
s-SEDiPA	$S_{28}E_{15}DiPA_{58}{}^{156}$	420/430	67	31.4 ± 0.3	260 ± 100	12 ± 2/10 ± 3
as-SEDiPA	$S_{38}E_{21}DiPA_{41}{}^{181}$	660/350	52	35.8 ± 0.3	480 ± 240	18 ± 4/9 ± 2
s-SEDMA	$S_{33}E_{17}DMA_{50}{}^{131}$	420/430	60	—	510 ± 310	18 ± 5/17 ± 5

[a] Subscripts denote the content of the respective polymer block in wt% and superscript denotes the number-average molecular weight in kg mol^{-1} determined by a combination of MALDI-ToF MS (matrix-assisted laser desorption/ionization – time of flight mass spectrometry) and ^{1}H NMR. [b] Hydrodynamic radii of the sCCMs determined by DLS. [c] Average sizes ± standard deviation as determined by TEM image analysis of at least 100 micelles/patches.

data were evaluated using ALV Correlator software (version V.3.0.0.17 10/2002) and the implemented ALV regularized fit option ($g2(t)$, CONTIN-analysis).

Results and discussion

Table 1 summarizes the molecular characteristics of the employed SEDxA triblock terpolymers, which were prepared by post-polymerization amidation of the PMMA block of the corresponding PS-*b*-PE-*b*-PMMA triblock terpolymers using *N*,*N*-dimethylethylenediamine and *N*,*N*-diisopropylethylenediamine, respectively.[43] Quantitative functionalization of the obtained SEDMA (polystyrene-*block*-polyethylene-*block*-poly(*N*,*N*-dimethylaminoethyl methacrylamide)) and SEDiPA (polystyrene-*block*-polyethylene-*block*-poly(*N*,*N*-diisopropylaminoethyl methacrylamide)) triblock terpolymers was confirmed by ^{1}H NMR

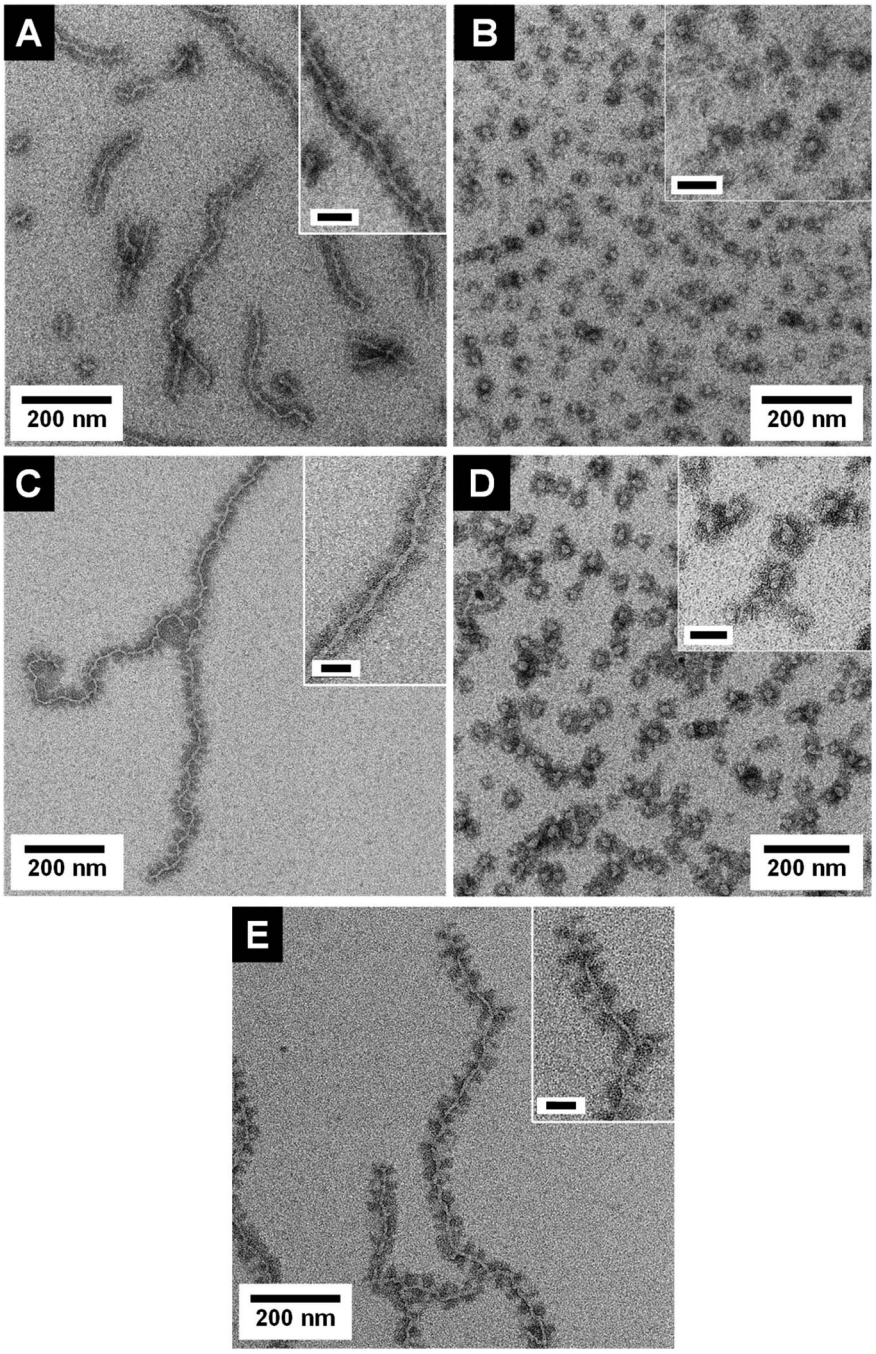

Fig. 2 TEM micrographs of $S_{28}E_{15}DiPA_{58}^{156}$ wCCMs ((A) s-SEDiPA(w)) and sCCMs ((B) s-SEDiPA(s)), $S_{38}E_{21}DiPA_{41}^{181}$ wCCMs ((C) as-SEDiPA(w)) and sCCMs ((D) as-SEDiPA(s)) and $S_{33}E_{17}DMA_{50}^{131}$ wCCMs ((E) s-SEDMA(w)). The PS domains were selectively stained with RuO_4 and appear dark. The inset in (D) shows at higher resolution RuO_2 nanoparticles formed by the reaction of the PS units with RuO_4 (oxidative cleavage of the phenyl rings). Scale bars in the insets are 50 nm.

(nuclear magnetic resonance) and FT-IR (Fourier transform-infrared) spectroscopy (Fig. S2 and S3†). The polarity of the amidated PDxA block was tuned by employing different amines for functionalization, whereas the patch sizes in the corona of the self-assembled crystalline-core micelles (CCMs) were altered using PS/PDxA blocks of different lengths. Consequently, triblock terpolymers with comparable block lengths of the PS and PDxA corona blocks are termed symmetric, *i.e.*, s-SEDiPA and s-SEDMA, and the triblock terpolymer with unequal block lengths is termed asymmetric, *i.e.*, as-SEDiPA.

The patchy CCMs with different shapes (worm-like and spherical) were obtained by CDSA of the functionalized triblock terpolymers.[60] First, the triblock terpolymers were dissolved above the melting point (T_m) of the polyethylene (PE) middle block using a selective (non-)solvent for the PE block, and then cooled down to the respective crystallization temperature (T_c) and, finally, crystallized at T_c for 24 h. Worm-like CCMs (wCCMs) are formed when a good solvent for the PE middle block (THF) is chosen, whereas a bad solvent for the PE block (1,4-dioxane) leads to the formation of spherical CCMs (sCCMs). The employed crystallization temperatures and respective μDSC (micro-differential scanning calorimetry) traces are given in the ESI (Table S1, Fig. S4†).

The transmission electron microscopy (TEM) micrographs shown in Fig. 2 as well as dynamic light scattering (DLS) results (Table 1, Fig. S8†) prove the successful formation of both micelle shapes, *i.e.*, patchy wCCMs and sCCMs. The sCCMs exhibit apparent hydrodynamic radii of $R_h \approx 31$–37 nm and the wCCMs show average lengths of $l \approx 260$–510 nm. Selective staining of the PS block with RuO_4 reveals the patchy structure of the corona for both micelle shapes. However, the patchy corona of the sCCMs is less defined compared to the well-ordered corona of the wCCMs, which shows an almost alternating arrangement of the PS (dark) and PDxA (bright) patches (Fig. 2). This is in agreement with our previous results on the corona structure of patchy PS-*b*-PE-*b*-PMMA triblock terpolymer micelles.[60] The size of the corona patches varies with the block length of the PS and PDxA corona blocks (Table 1), *i.e.*, the widths of both corona patches are similar for a symmetric composition of the corona in terms of PS and PDxA block lengths ($\approx$18 nm for s-SEDMA and $\approx$11 nm for s-SEDiPA wCCMs, respectively), but show a significant difference for an asymmetric block length ratio ($\approx$18 nm for PS and $\approx$9 nm for PDiPA in the case of as-SEDiPA wCCMs).

The functional patchy micelles were then used in a coaxial electrospinning process to generate nonwovens with a patch-like surface structure (Fig. 1A), employing a PS solution ($M_n = 1.8\ 10^6$ g mol^{-1}, $c = 7$ wt% in DMF) as the core-forming material and a dispersion of the patchy micelles as the shell ($c = 10$ g L^{-1} in THF (wCCMs) or dioxane (sCCMs)). The patchy nonwovens are termed according to the micelle type employed as the shell material, *i.e.*, NW_s-SEDiPA(w) stands for a nonwoven with s-SEDiPA wCCMs on the surface. The resulting fibres show an uniform thickness of 1.27 ± 0.15 μm and a homogeneous coating of the surface with the functionalized CCMs (Fig. 3A–C, 8A and S9†), as revealed by scanning electron microscopy (SEM). This is promoted by the PS patches of the micelles, which are adsorbed onto the surface of the PS nonwoven. The characteristic shape of the sCCMs (Fig. 3A and S9B†) as well as wCCMs (Fig. 3B, 8A and S9A†) was preserved after

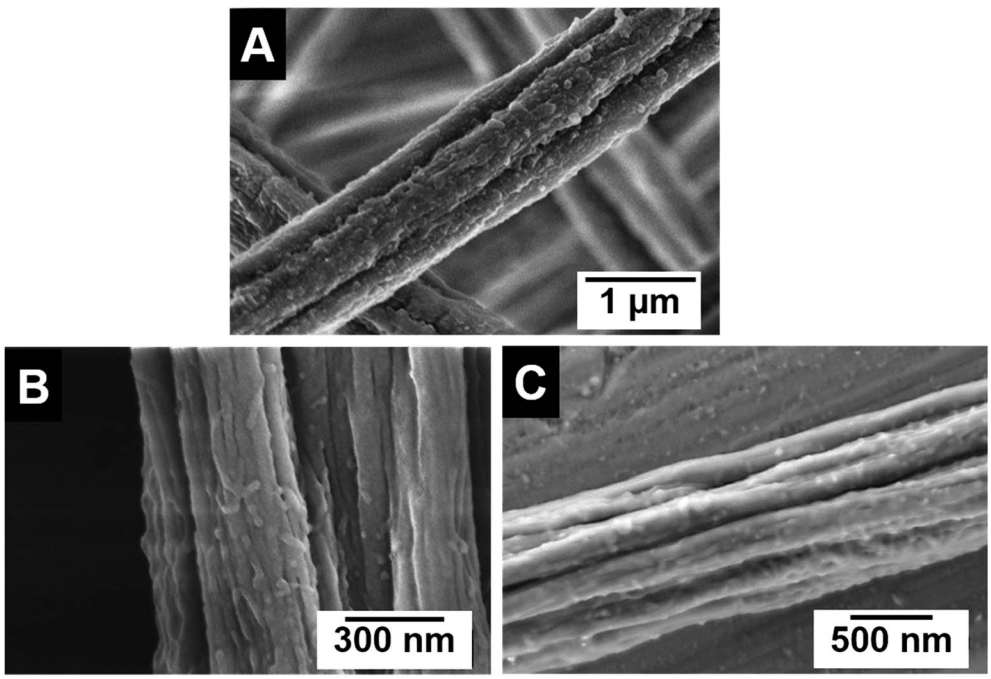

Fig. 3 SEM micrographs of patchy nonwovens based on s-SEDiPA sCCMs ((A) NW_s-SEDiPA(s)) and wCCMs ((B and C) NW_s-SEDiPA(w)). The SEM image in (C) was acquired on an uncoated sample of NW_s-SEDiPA(w), employing the beam deceleration mode (for details see the Experimental section).

Table 2 Au content and overall surface area of embedded Au NPs in the hybrid nonwovens

Hybrid nonwoven	$m_{Au,calibration}$ [a,b] [μg cm^{-2}]	$m_{Au,UV\text{-}vis\ 400\ nm}$ [a,c] [μg cm^{-2}]	S_{AuNP} [d] [m^2]
NW_s-SEDiPA(s)/Au	69	70	$(2.29 \pm 0.58) \times 10^{-3}$
NW_s-SEDiPA(w)/Au	52	57	$(1.86 \pm 0.47) \times 10^{-3}$
NW_as-SEDiPA(s)/Au	77	77	$(2.52 \pm 0.64) \times 10^{-3}$
NW_as-SEDiPA(w)/Au	82	82	$(2.68 \pm 0.68) \times 10^{-3}$
NW_s-SEDMA(w)/Au	76	77	$(2.52 \pm 0.64) \times 10^{-3}$

[a] Relative to the area of the nonwoven ($S = 1$ cm^2) under the assumption of an equal thickness ($d \approx 400$ μm). [b] The amount of Au in the dispersions was calculated according to Fig. S5, using a calibration based on the employed Au NP dispersion. [c] Determined from the absorbance at $\lambda = 400$ nm according to eqn (S1). [d] Overall surface area of the embedded Au NPs calculated from the NP diameter obtained by TEM ($D_{TEM} = 9.5 \pm 2.4$ nm) and the Au content in the hybrid nonwovens ($m_{Au,UV\text{-}vis\ 400\ nm}$), assuming a perfect spherical shape (eqn (S7–S10)). Given errors were calculated based on error propagation (eqn (S11)).

electrospinning, as indicated by spherical and elongated structures observable on the fibres' surface. In order to exclude any effect arising from the sample preparation for SEM, *i.e.*, coating with a thin Pt layer ($d \approx 1.3$ nm), we have measured one uncoated patchy nonwoven based on s-SEDiPA wCCMs (NW_s-SEDiPA(w), Fig. 3C). Here, the so-called beam deceleration mode was employed (for details see the Experimental section) and again worm-like structures arising from the decoration of the PS fibres with wCCMs are visible, showing that coating with Pt has no impact on the observed fibre morphology.

In the next step, Au NP-containing hybrid nonwovens were produced *via* a facile ligand exchange process (Fig. 1B), *i.e.*, the patchy nonwovens (surface area: $S = 1$ cm^2 and thickness: $d \approx 400$ μm) were dipped in an aqueous dispersion of preformed, citrate-stabilized Au NPs for 24 h and subsequently washed with sodium citrate solution and water to remove unbound Au NPs. The employed Au NPs showed a rather broad size distribution with a number average diameter of $D_{TEM} = 9.5 \pm 2.4$ nm, as determined by TEM (Fig. S1A and B†). This was also confirmed by asymmetric flow field-flow fractionation (AF4), revealing a tailing of the size distribution toward larger particle sizes (Fig. S1D†). The obtained average diameter of gyration of $D_g =$

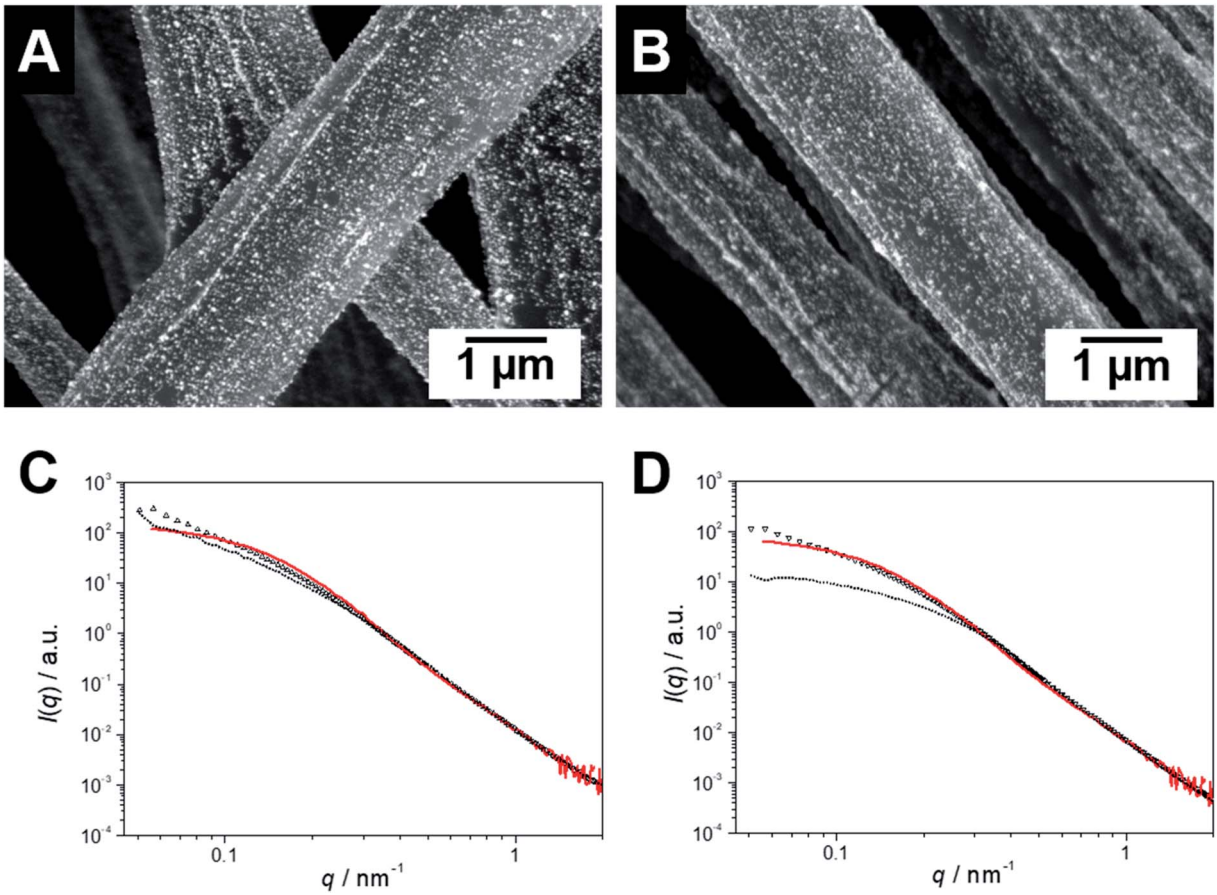

Fig. 4 SEM micrographs of Au NP-loaded patchy nonwovens based on s-SEDiPA wCCMs ((A) NW_s-SEDiPA(w)/Au) and sCCMs ((B) NW_s-SEDiPA(s)/Au), analysed with a BSE detector; the Au NPs appear as bright dots. SAXS profiles of the Au NPs immobilized in patchy nonwovens based on s-SEDiPA wCCMs ((C) NW_s-SEDiPA(w)/Au) and sCCMs ((D) NW_s-SEDiPA(s)/Au), prior to (open triangles) and after 10 catalysis cycles (doted profiles). The SAXS profile of the corresponding aqueous Au NP dispersion employed for the dipping process is shown in red and was shifted vertically to match the scattering intensity of the Au NPs in the respective hybrid nonwovens in the high q-range to facilitate comparison.

17.9 ± 2 nm agrees with the size determined by TEM (D_{TEM} = 9.5 ± 2.4 nm), taking the rather broad size distribution and the fact that light scattering overestimates the content of larger particles (scattering intensity is proportional to D^6) into account. It is noted that we intentionally did not aim for the production of narrowly distributed Au NPs, as for catalytic applications a simple and fast NP synthesis is preferred.

The successful incorporation of Au NPs within the functional surface of the patchy nonwovens could be easily followed by the discoloration of the Au NP dispersion and the resulting purple colour of the produced hybrid nonwovens. The strong binding of the Au NPs within the functional surface patches can be attributed to a replacement of the citrate ligands by the multidentate, amino-group containing patches (gain in entropy by release of citrate molecules). Electrostatic interactions with the amino groups ($pK_a \approx 7$) in the functional patches can be neglected as the Au NP dispersion shows a pH of 8 and under these conditions the amino groups are uncharged.[68] The Au content of the hybrid nonwovens was calculated from the respective Au content of the Au NP dispersions after loading, as determined by UV-vis (ultraviolet-visible) spectroscopy. Here, the Au content of the initial Au NP dispersion determined by ICP-OES (inductively coupled plasma-optical emission spectrometry) was used as the reference (difference method). A detailed description of this method is given in the ESI (Fig. S5†). The Au contents of the hybrid nonwovens and the overall surface area (S_{AuNP}) of the embedded Au NPs, as determined from the respective Au content and the average diameter of D_{TEM} = 9.5 ± 2.4 nm, are given in Table 2. The Au NP-loaded hybrid nonwovens are termed according to the employed patchy nonwoven template, *i.e.*, NW_s-SEDiPA(w)/Au stands for a patchy NW_s-SEDiPA(w) nonwoven loaded with Au NPs.

An important issue in heterogeneous catalysis with supported NPs is the efficient immobilization and stabilization of the NPs in order to avoid agglomeration and, thus, a loss in the catalytically active surface area, while preserving the catalytic activity of the NPs. The latter might be strongly influenced by the type of stabilizing ligand, *i.e.*, their binding strength to the Au NPs' surface. Accordingly, the performance of the patchy nonwovens as a support for the efficient stabilization of Au NPs was analysed by SEM and SAXS (small-angle X-ray scattering), and the catalytic activity of the immobilized NPs was probed employing the alcoholysis of dimethylphenylsilane. In the following, the impact of the micelle morphology and patch size as well as patch chemistry will be discussed in detail.

Effect of micelle morphology and patch size

SEM coupled with a backscattered electron (BSE) detector confirms the homogeneous loading of the patchy nonwovens based on spherical and worm-like s-SEDiPA CCMs with Au NPs (Fig. 4A and B). NP agglomerates, which would be discernible as large, bright appearing domains, are hardly detectable. The absence of larger NP agglomerates is also supported by the SAXS results shown in Fig. 4C (NW_s-SEDiPA(w)/Au) and Fig. 4D (NW_s-SEDiPA(s)/Au), which compare the scattering profiles of the Au NPs within the hybrid nonwovens (open triangles) with that of the Au NP dispersion (coloured in red) used in the loading process. The scattering profiles of the embedded Au NPs were determined by subtracting the scattering intensity of the Au NP-loaded hybrid nonwovens from that of the corresponding neat nonwovens, as described in our previous work.[68] For both hybrid nonwovens, the scattering profile of the embedded Au NPs is similar to that of the neat Au NP dispersion for scattering vectors $q > 0.1$ nm^{-1}. Only for smaller q-values, the scattering profiles do not reach a plateau but show a slight increase with decreasing q-values. This might point to a weak, partial agglomeration of the incorporated Au NPs or to an additional structure factor contribution due to the close vicinity of the embedded Au NPs in the corona of the patchy micelles located on the nonwovens' surface.

We have also studied whether agglomeration or a loss of the embedded Au NPs might occur during catalysis. For the hybrid nonwoven based on s-SEDiPA wCCMs (Fig. 4C, NW_s-SEDiPA(w)/Au) the scattering profiles prior to (open triangles) and after 10 catalysis cycles (dotted profile) are nearly identical, *i.e.*, neither a loss of Au NPs (scattering intensity would decrease) nor a significant agglomeration (steeper increase of scattering intensity for low q-values would be expected) takes place during catalysis. In contrast, for the hybrid nonwoven based on s-SEDiPA sCCMs (Fig. 4D, NW_s-SEDiPA(s)/Au) a significantly lower scattering intensity and a pronounced plateau for low q-values were observed after 10 catalysis cycles. This points to a partial loss of larger Au NPs during catalysis, revealing that patchy nonwovens based on spherical s-SEDiPA CCMs are less efficient in NP stabilization with respect to s-SEDiPA wCCMs. This might be attributed to the less defined patchy corona of the sCCMs (Fig. 2).

Fig. 5 displays the scattering profiles of the embedded Au NPs for hybrid nonwovens based on spherical (NW_as-SEDiPA(s)/Au, filled squares) and worm-like (NW_as-SEDiPA(w)/Au, open triangles) as-SEDiPA CCMs, which exhibit

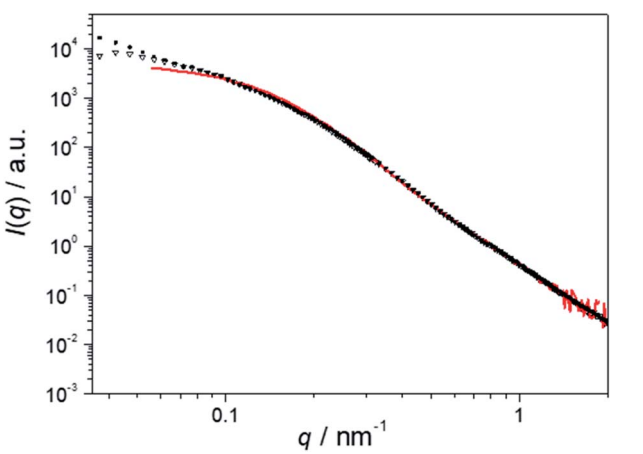

Fig. 5 SAXS profiles of the Au NPs immobilized in patchy nonwovens based on as-SEDiPA wCCMs (NW_as-SEDiPA(w)/Au, open triangles) and sCCMs (NW_as-SEDiPA(s)/Au, filled squares). The SAXS profile of the corresponding aqueous Au NP dispersion employed for the dipping process is shown in red and was shifted vertically to match the scattering intensity of the Au NPs in the respective hybrid nonwovens in the high q-range to facilitate comparison.

a highly asymmetric corona, *i.e.*, different PS and PDiPA patch sizes (Table 1). Here, the scattering intensity for NW_as-SEDiPA(w)/Au shows only a comparably weak increase for low q-values and tends to form a plateau, unlike the behaviour of NW_s-SEDiPA(w)/Au (symmetric corona). Moreover, the scattering profile of the embedded Au NPs is now almost identical to that of the Au NPs in the initial Au NP dispersion (red profile). This points to a more efficient stabilization of the Au NPs embedded within the asymmetric patchy corona of as-SEDiPA wCCMs against agglomeration. Again, for the NW_as-SEDiPA(s)/Au hybrid nonwoven a steeper increase in scattering intensity for low q-values is observed, which points to a partial agglomeration and underpins the conclusion that patchy sCCMs are less efficient in NP stabilization compared to wCCMs. The enhanced stabilization of Au NPs against agglomeration for as-SEDiPA wCCMs might be attributed to the slightly smaller size of the functional PDiPA patches (9 ± 2 nm for as-SEDiPA(w) and 10 ± 3 nm for s-SEDiPA(w)) in combination with the increased size of the PS patches (18 ± 4 nm for as-SEDiPA(w) and 12 ± 2 nm for s-SEDiPA(w)), which separate the PDiPA patches from each other (Table 1). Accordingly, there is less space for the Au NPs in the PDiPA patches and the spatial separation of the PDiPA patches by the PS patches is stronger, leading to a reduced possibility to form NP agglomerates.

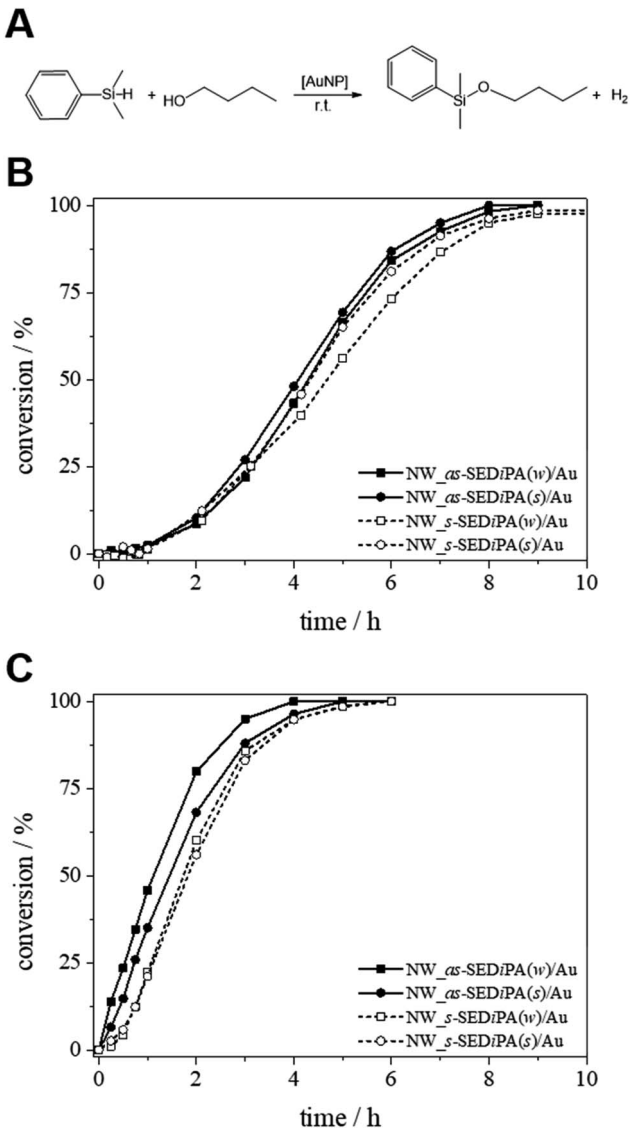

Fig. 6 (A) Au NP-catalysed alcoholysis of dimethylphenylsilane in n-BuOH. Corresponding conversion *vs.* time plots employing different Au NP-loaded patchy nonwovens based on s- and as-SEDiPA CCMs as catalysts ((B) 1st cycles; (C) 10th cycles).

Next, we studied the impact of the micelle shape and patch size on the catalytic activity of the patchy hybrid nonwovens, employing the alcoholysis of dimethylphenylsilane in n-butanol (n-BuOH) as an established model reaction (Fig. 6A).[68] We ran 10 consecutive cycles and the kinetics were followed for the 1st and 10th cycles in order to address the effect of swelling of the PDxA patches in n-BuOH on the catalytic performance and to probe the reusability of our catalyst system. Detailed information on the Au content of the nonwovens is given in Table 2, and the used molar ratio of Au to dimethylphenylsilane and other kinetic parameters are summarized in Table 3.

Fig. 6B shows the conversion *vs.* time (x_p/t) plots of the 1st catalysis cycles for hybrid nonwovens based on s- and as-SEDiPA CCMs. Irrespective of the micelle morphology and patch sizes of the CCMs employed for surface decoration, the hybrid nonwovens showed an induction time of $t_{ind} \approx 1$ h. Full conversion is reached in about 8–9 h for all hybrid nonwovens, while the s-SEDiPA based systems show slightly longer reaction times. The latter might be attributed to the higher PDiPA content in the corona of the s-SEDiPA micelles in combination with a higher PDiPA block length (Table 1), resulting in a slightly higher diffusion barrier for the reactants in the swollen PDiPA patches with respect to as-SEDiPA based hybrid nonwovens. However, one has to take the slightly different Au contents of the hybrid nonwovens into account (Table 2). This point will be addressed in detail later on in the discussion of the kinetics of the 10th catalysis cycles. Interestingly, the induction times are significantly decreased for the 10th catalysis cycles ($t_{ind} \approx$ 10–20 min, Table 3) and, in addition, full conversion is already reached in about 4–6 h. This shows that the higher induction and reaction times observed in the 1st catalysis cycles are most likely related to an initial period, where the PDiPA patches swell in n-BuOH and, thus, enable the reactants to access the embedded Au NPs. This is also in contrast to our previous work, where we have observed that the 1st and 10th catalysis cycles were almost identical with comparable induction times.[68] This discrepancy can be attributed to the different degrees of functionalization (f) of the PDiPA blocks (f = 55% *vs.* quantitative functionalization in this study) and the fact that the previously employed amidation method resulted in about 50 mol% imide units, which show only limited solubility in n-BuOH. Hence, the swelling of the PDiPA patches clearly affects the accessibility of the catalytically active Au NP surface and, as a consequence, the duration of the induction period and the overall reaction time.

In order to get a deeper insight into the kinetics of the reaction and, hence, the influence of the micelle shape and patch size, we have evaluated the kinetics of the 10th catalysis

Table 3 Kinetic parameters for the 10th cycles of the catalytic alcoholysis of dimethylphenylsilane in *n*-BuOH, obtained using our extended pseudo 1st order kinetics model given in eqn (5)

Hybrid nonwovens	Au[a] mol%	k_{app}[b] [h^{-1}]	r [h^{-1}]	t_{ind}[c] [min]	t_R[d] [h]	k[e] [L m^{-2} mol^{-1} s^{-1}]
NW_s-SEDiPA(s)/Au	0.15	1.77 ± 0.10	0.29 ± 0.02	21	5.29	(1.97 ± 0.51) × 10^{-2}
NW_s-SEDiPA(w)/Au	0.12	1.54 ± 0.11	0.38 ± 0.05	20	5.25	(2.10 ± 0.55) × 10^{-2}
NW_as-SEDiPA(s)/Au	0.17	1.18 ± 0.10	0.79 ± 0.15	16	5.16	(1.19 ± 0.31) × 10^{-2}
NW_as-SEDiPA(w)/Au	0.18	1.27 ± 0.11	1.43 ± 0.38	11	4.32	(1.20 ± 0.32) × 10^{-2}
NW_s-SEDMA(w)/Au	0.17	1.55 ± 0.26	0.54 ± 0.16	17	4.68	(1.56 ± 0.47) × 10^{-2}

[a] Relative to dimethylphenylsilane (0.23 mmol). [b] Apparent rate constant (k_{app}) and accessibility rate (r) determined according to eqn (5). [c] Time at 3% conversion was taken as the induction time (t_{ind}) and calculated using eqn (5). [d] Reaction time (t_R) at 99% conversion, calculated using eqn (5). [e] Rate constant normalized to the overall surface area of the embedded Au NPs (S_{AuNP}, Table 2) and the concentration of *n*-BuOH ($c_{n\text{-BuOH}}$ = 10.93 mol L^{-1}); given errors were calculated based on error propagation (eqn (S12)).

cycles. We have purposely chosen the 10th catalysis cycles to rule out the effect of initial swelling from the dry state, manifested by the long induction times observed for the 1st catalysis cycles. Despite the large excess of *n*-BuOH compared to silane, Fig. S10† shows that a classical pseudo 1st order kinetics model cannot reproduce the experimental data over the full time range. We therefore developed a theoretical model, which extends the classical pseudo 1st order kinetics with an additional induction period to address the influence of patch swelling. We consider the reaction of dimethylphenylsilane (reactant E) with *n*-BuOH, which acts as both the solvent and the reactant, employing the rate law

$$\frac{d[E]}{dt} = -\kappa(t)[E][n\text{-BuOH}]. \quad (1)$$

In order to model the induction period, *i.e.*, the swelling of the patches, the two reactants (dimethylphenylsilane and *n*-BuOH) are considered to become available for the embedded catalytically active Au NPs with a certain accessibility rate r. The specialty of our model is that the reaction rate $\kappa(t)$ is increasing over time according to

$$\kappa(t) = \kappa_0(1 - e^{-rt}), \quad (2)$$

representing the slowly increasing availability of the reactants over the time t. The accessibility rate r is a measure of how quickly this process occurs.

Replacing (2) in (1) yields the rate law for our model

$$\frac{d[E]}{dt} = -k_{app}(1 - e^{-rt})[E], \quad (3)$$

where $k_{app} = \kappa_0[n\text{-BuOH}]$ is the apparent rate constant. Separating variables and integrating eqn (3) lead to

$$-\int_{[E_0]}^{[E]} \frac{1}{[E']} d[E'] = \int_0^t k_{app}\left(1 - e^{-rt'}\right) dt'. \quad (4)$$

The natural logarithm form of the power law expression is finally obtained as

$$-\ln\frac{[E]}{[E]_0} = k_{app}\left(\frac{e^{-rt}}{r} + t\right) - \frac{k_{app}}{r}. \quad (5)$$

We note that for the immediate availability of the reactants, *i.e.*, $r \to \infty$, the classic equation describing the kinetics of a pseudo 1st order reaction (eqn (S5)†) is recovered from eqn (5).

Accordingly, the experimental data were fitted with eqn (5) to yield the apparent rate constants (k_{app}) and the accessibility rates (r) (Fig. 7 and S11†). To facilitate comparison between the different catalyst systems the apparent rate constants were normalized to the concentration of *n*-BuOH ($c_{n\text{-BuOH}}$ = 10.93 mol L^{-1}) and the overall surface area (S_{AuNP}) of the embedded Au NPs, yielding the rate constants k for the Au NP-catalysed alcoholysis of dimethylphenylsilane (eqn (S6),† Table 3). Using the obtained values for k_{app} and r, the corresponding induction times (t_{ind}) and overall reaction times (t_R) can be calculated from eqn (5) and are also given in Table 3.

The normalized rate constants (k) are in a comparable range for the different hybrid nonwovens based on s-SEDiPA and as-SEDiPA CCMs (Table 3). Similar results were obtained by using the classical 1st order kinetics model for the determination of the reaction rate constants (eqn (S5), Fig. S10, Table S2†), although in this case only the second half of the observation period, where the plot exhibits a constant slope, can be fitted by the classical model. Interestingly, the accessibility parameters

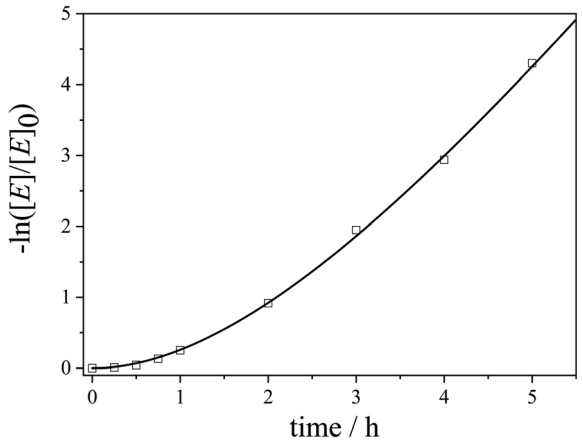

Fig. 7 Kinetics plot for the 10th cycle of the catalytic alcoholysis of dimethylphenylsilane with an Au NP-loaded patchy nonwoven based on s-SEDiPA wCCMs (NW_s-SEDiPA(w)/Au) as the catalyst (squares: experimental data and line: fit according to our extended pseudo 1st order kinetics model in eqn (5)).

(r) for the as-SEDiPA based hybrid nonwovens are higher with respect to those of the s-SEDiPA based ones. A possible explanation is the lower steric demand of the PDiPA patches in the as-SEDiPA CCMs (lower PDiPA block length and content in the corona, Table 1). This is also reflected in the shorter induction and reaction times observed for the as-SEDiPA based hybrid nonwovens, despite their slightly lower normalized rate constants compared to s-SEDiPA based nonwovens. Altogether, the induction ($t_{ind} \approx$ 10–20 min) and reaction times ($t_R \approx$ 4–5 h) for the 10th catalysis cycles (Table 3) are significantly shorter in comparison to the 1st catalysis cycles ($t_{ind} \approx$ 1 h and $t_R \approx$ 8–9 h, as estimated from the x_p/t plots in Fig. 6B), showing again the importance of patch swelling in n-BuOH for the reaction kinetics. With respect to our previous work a significant reduction of the reaction time from about 7 to 4.3 h could be achieved for the NW_as-SEDiPA(w)/Au hybrid nonwoven.[68]

Effect of patch chemistry

To further study the effect of patch swelling on the catalytic activity of the hybrid nonwovens, we altered the patch chemistry (PDMA *vs.* PDiPA) and compared nonwovens decorated with s-SEDiPA (Fig. 3B and C) and s-SEDMA (Fig. 8A) wCCMs. If there is any effect of patch chemistry on the reaction kinetics, this effect should be largest for the CCMs with the highest weight fraction of PDxA units in the corona, *i.e.*, s-SEDMA and s-SEDiPA (Table 1). The PDMA patches are more hydrophilic compared to PDiPA and, consequently, are expected to swell faster and to a greater extend in n-BuOH.

The SEM image acquired with a BSE detector again shows nicely dispersed, bright appearing Au NPs on the surface of the respective NW_s-SEDMA(w)/Au hybrid nonwoven (Fig. 8B). The SAXS profile of the embedded Au NPs (Fig. 8C, filled squares) shows no sign of agglomeration, in contrast to the weak, partial agglomeration observed for the s-SEDiPA (Fig. 4C and D) and as-SEDiPA (Fig. 5) based hybrid nonwovens. The scattering profile is almost identical to that of the Au NPs in the initial NP dispersion (Fig. 8C, red profile) and the scattering intensity reaches a well-defined plateau for low q-values. This shows that nonwovens decorated with s-SEDMA wCCMs are best suited for Au NP stabilization and efficiently hinder the formation of NP agglomerates.

Fig. 8D compares the x_p/t-plots for the 1st and 10th cycles of the catalytic alcoholysis of dimethylphenylsilane with NW_s-

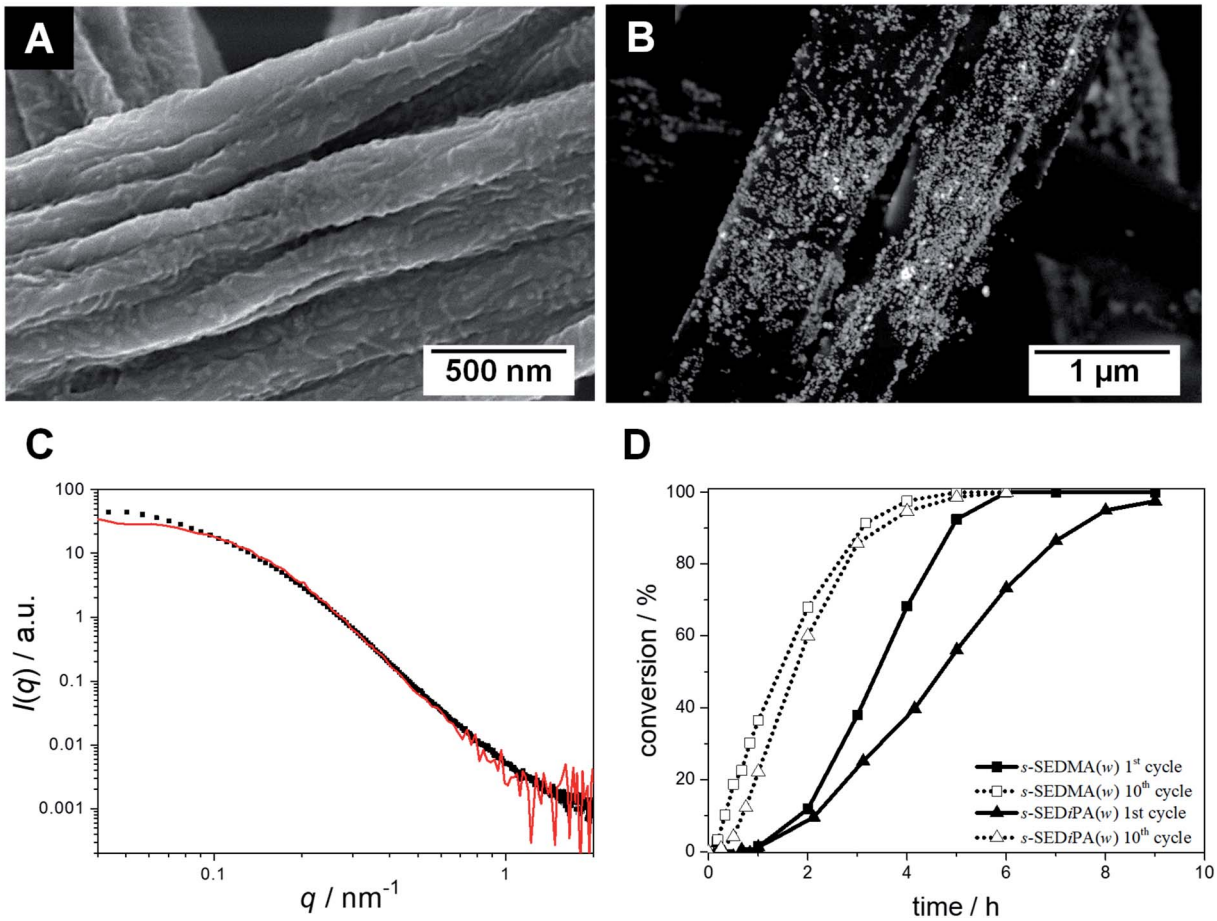

Fig. 8 SEM micrographs of neat (A) and Au NP-loaded ((B) BSE detector) patchy nonwovens based on s-SEDMA(w) (NW_s-SEDMA(w)/Au); the Au NPs in (B) appear as bright dots. (C) SAXS profiles of the Au NPs immobilized in the patchy nonwoven (filled squares) and of the corresponding aqueous Au NP dispersion employed for the dipping process (red). (D) Comparison of conversion *vs.* time plots (1st and 10th cycles) for the catalytic alcoholysis of dimethylphenylsilane with Au NP-loaded patchy nonwovens based on s-SEDiPA (NW_s-SEDiPA(w)/Au) and s-SEDMA (NW_s-SEDMA(w)/Au) wCCMs as catalysts.

SEDiPA(w)/Au and NW_s-SEDMA(w)/Au, respectively. The most obvious difference can be observed in the 1st catalysis cycles. The induction times are comparable ($t_{ind} \approx 1$ h), but the overall reaction time is significantly lower for the s-SEDMA(w) based hybrid nonwoven (about 6 h compared to 9 h for NW_s-SEDiPA(w)/Au). In addition, for the 10th cycles the accessibility parameter (r) is higher and the induction (t_{ind}) as well as overall reaction time (t_R) are lower for the s-SEDMA(w) decorated hybrid nonwoven (Table 3). This clearly underlines the influence of patch swelling on the reaction kinetics and supports our assumption that the increased hydrophilicity of the PDMA patches results in a better swelling of the patches in *n*-BuOH (higher accessibility parameter) and, thus, leads to reduced induction and reaction times.

In summary, concerning the efficiency for Au NP stabilization patchy wCCMs are more efficient compared to sCCMs and the s-SEDMA(w) based nonwoven showed the best performance, *i.e.*, no hints of NP agglomeration could be detected by SEM and SAXS. However, the shortest induction and reaction times for the 10th cycle of the Au NP-catalyzed alcoholysis of dimethylphenylsilane were observed for the as-SEDiPA(w) based hybrid nonwoven. Accordingly, the interplay of the micelle shape, patch size and chemistry influences the stabilization and catalytic activity of the embedded Au NPs. PDMA patches are more efficient for NP stabilization, which might be attributed to a stronger interaction with the NPs' surface (less steric hindrance of methyl groups compared to iso-propyl groups). But in contrast, a stronger interaction with the NPs' surface could lead to reduced reaction rate constants (Table 3: NW_s-SEDMA(w)/Au shows a slightly lower normalized rate constant (k) compared to NW_s-SEDiPA(w)/Au). Besides these parameters, also the accessibility parameter (r) has to be taken into account, which describes the rate at which the reactants (dimethylphenylsilane and *n*-BuOH) become available for the embedded Au NPs. This parameter is largest for NW_as-SEDiPA(w)/Au and results in the shortest observed induction and reaction times, despite the lower normalized rate constant in comparison to s-SEDMA(w) and s-SEDiPA(w) based hybrid nonwovens (Table 3).

The reaction times for full conversion and the rate constants strongly depend on the Au content and the Au NP size, *i.e.*, the total Au NP surface area. This makes a comparison to other studies difficult, as mostly only reaction times are given and the rate constants are not normalized to the overall Au NP surface area. Nevertheless, the reported reaction times for the Au NP-catalysed alcoholysis of dimethylphenylsilane with *n*-BuOH at room temperature are in the range of the reaction times found in this study ($t_R \approx$ 4–5 h) or even higher (Table S3†).[70,73,74] Shorter reaction times at full conversion were only reported for Au NPs supported on nanosized hydroxyapatite (Au/HAP_{nano}) and were attributed to the high adsorption capacity of the support, which increases locally the concentration of dimethylphenylsilane at the surface of Au/HAP_{nano}.[75] However, the employed Au NPs (D = 3 nm) were significantly smaller compared to the Au NPs used in this study ($D_{TEM} = 9.5 \pm 2.4$ nm), which results in an increased catalytically active surface area.

Conclusions

The studied electrospun patchy nonwovens are efficient supports for the stabilization of Au NPs against agglomeration and the corresponding hybrid nonwovens with embedded Au NPs exhibit a high activity and reusability in the catalytic alcoholysis of dimethylphenylsilane. Utilizing an extended pseudo 1st order kinetics model revealed that the catalytic activity is influenced by the patch size and chemistry (PDMA *vs.* PDiPA patches), which determine the accessibility of the reactants to the surface of the embedded Au NPs. This is also manifested by the observation of longer induction and reaction times in the 1st catalysis cycles in comparison to that of the 10th cycles. This allows tailoring the properties of the patchy hybrid nonwovens in terms of NP stabilization and catalytic performance. Compared to heterogeneous catalysis with Au NPs that are stabilized by particulate supports (MOFs, metal oxides, and 2D materials) our "*tea-bag*"-like catalyst system can be simply dipped in the reaction mixture and pulled out after catalysis without the need for filtration or centrifugation to separate the catalyst. Electrospinning as a "*top-down*" approach can be easily upscaled and the synthesis of the PS-*b*-PE-*b*-PMMA precursor triblock terpolymers (catalytic hydrogenation of polystyrene-*block*-polybutadiene-*block*-poly(methyl methacrylate) triblock terpolymers produced by living anionic polymerization (also commercially available from Arkema)) can be conducted on a kg scale. In addition, the functional, amino group-containing patches are not only efficient stabilizers for Au NPs, but can also be employed for the incorporation of other metal (Ag and Pd) or transition metal oxide (CuO and ZnO) NPs. This opens the way for a variety of applications in heterogeneous catalysis, which will be addressed in future studies. Moreover, the facile loading of the patchy nonwovens by a simple dipping process and the efficient stabilization of the embedded NPs might also be utilized for water purification.

Conflicts of interest

There are no conflicts to declare.

Acknowledgements

This work was supported by the German Research Foundation through the Collaborative Research Centre SFB 840 (projects A2, A12 and B8) and the Bavarian State Ministry of the Environment and Consumer Protection (TNT01NaT-72524). We thank S. Agarwal for assistance with coaxial electrospinning and H.-W. Schmidt for discussion and support in SEM measurements. We appreciate the support of the Keylab Mesoscale Characterization: Scattering Techniques (S. Rosenfeldt) of the Bavarian Polymer Institute (BPI) for conducting some of the SAXS experiments, Carmen Kunert for SEM and TEM and Rika Schneider for AF4 measurements. C. H. acknowledges support by the Graduate School of the University of Bayreuth. G. S. acknowledges support from the Biological Physics program of the Elite Network of Bavaria and S. G. thanks the Volkswagen Foundation. We appreciate support through the computational resources provided by the Bavarian Polymer Institute.

References

1 A. Alshammari and V. N. Kalevaru, in *Catalytic Application of Nano-Gold Catalysts*, ed. N. K. Mishra, InTech, 2016.
2 M. Haruta, *Chem. Rec.*, 2003, **3**, 75–87.
3 S. Nishimura and K. Ebitani, *ChemCatChem*, 2016, **8**, 2303–2316.
4 C. Burda, X. Chen, R. Narayanan and M. A. El-Sayed, *Chem. Rev.*, 2005, **105**, 1025–1102.
5 M. Stratakis and H. Garcia, *Chem. Rev.*, 2012, **112**, 4469–4506.
6 G. C. Bond, P. A. Sermon, G. Webb, D. A. Buchanan and P. B. Wells, *J. Chem. Soc., Chem. Commun.*, 1973, 444–445.
7 M. Haruta, T. Kobayashi, H. Sano and N. Yamada, *Chem. Lett.*, 1987, **16**, 405–408.
8 L. M. Rossi, J. L. Fiorio, M. A. S. Garcia and C. P. Ferraz, *Dalton Trans.*, 2018, **47**, 5889–5915.
9 S. Kunz, *Top. Catal.*, 2016, **59**, 1671–1685.
10 Á. Molnár and A. Papp, *Coord. Chem. Rev.*, 2017, **349**, 1–65.
11 A. Cao, R. Lu and G. Veser, *Phys. Chem. Chem. Phys.*, 2010, **12**, 13499–13510.
12 M. Davidson, Y. Ji, G. J. Leong, N. C. Kovach, B. G. Trewyn and R. M. Richards, *ACS Appl. Nano Mater.*, 2018, **1**, 4386–4400.
13 I. Ro, J. Resasco and P. Christopher, *ACS Catal.*, 2018, **8**, 7368–7387.
14 Y. Wang, H. Arandiyan, J. Scott, A. Bagheri, H. Dai and R. Amal, *J. Mater. Chem. A*, 2017, **5**, 8825–8846.
15 G. Zhan and H. C. Zeng, *Coord. Chem. Rev.*, 2016, **320–321**, 181–192.
16 M. Massaro, C. G. Colletti, G. Lazzara, S. Milioto, R. Noto and S. Riela, *J. Mater. Chem. A*, 2017, **5**, 13276–13293.
17 J. Yuan, H. Schmalz, Y. Xu, N. Miyajima, M. Drechsler, M. W. Möller, F. Schacher and A. H. E. Müller, *Adv. Mater.*, 2008, **20**, 947–952.
18 J. John, E. Gravel, A. Hagège, H. Li, T. Gacoin and E. Doris, *Angew. Chem., Int. Ed.*, 2011, **50**, 7533–7536.
19 Y. Gong, M. Li, H. Li and Y. Wang, *Green Chem.*, 2015, **17**, 715–736.
20 A. Kumar and Q. Xu, *ChemNanoMat*, 2018, **4**, 28–40.
21 S. Navalon, A. Dhakshinamoorthy, M. Alvaro and H. Garcia, *Coord. Chem. Rev.*, 2016, **312**, 99–148.
22 R. K. Sharma, S. Dutta, S. Sharma, R. Zboril, R. S. Varma and M. B. Gawande, *Green Chem.*, 2016, **18**, 3184–3209.
23 H. R. Moon, D.-W. Lim and M. P. Suh, *Chem. Soc. Rev.*, 2013, **42**, 1807–1824.
24 C. R. Kim, T. Uemura and S. Kitagawa, *Chem. Soc. Rev.*, 2016, **45**, 3828–3845.
25 A. Dhakshinamoorthy, A. M. Asiri and H. Garcia, *ACS Catal.*, 2017, **7**, 2896–2919.
26 M. Kaushik and A. Moores, *Green Chem.*, 2016, **18**, 622–637.
27 M. Rose, *ChemCatChem*, 2014, **122**, 1166–1182.
28 J. Artz, *ChemCatChem*, 2018, **10**, 1753–1771.
29 S. Bhattacharyya, D. Samanta, S. Roy, V. P. Haveri Radhakantha and T. K. Maji, *ACS Appl. Mater. Interfaces*, 2019, **11**, 5455–5461.
30 J. He, S. Razzaque, S. Jin, I. Hussain and B. Tan, *ACS Appl. Nano Mater.*, 2019, **2**, 546–553.
31 S. K. Dey, D. Dietrich, S. Wegner, B. Gil-Hernández, S. S. Harmalkar, N. de Sousa Amadeu and C. Janiak, *ChemistrySelect*, 2018, **3**, 1365–1370.
32 Z. H. Farooqi, S. R. Khan and R. Begum, *Mater. Sci. Technol.*, 2017, **33**, 129–137.
33 R. Roa, S. Angioletti-Uberti, Y. Lu, J. Dzubiella, F. Piazza and M. Ballauff, *Z. Phys. Chem.*, 2018, **232**, 773–803.
34 Y. Lu and M. Ballauff, *Prog. Polym. Sci.*, 2016, **59**, 86–104.
35 P. Hervés, M. Pérez-Lorenzo, L. M. Liz-Marzán, J. Dzubiella, Y. Lu and M. Ballauff, *Chem. Soc. Rev.*, 2012, **41**, 5577–5587.
36 M. Müllner and A. H. E. Müller, *Polymer*, 2016, **98**, 389–401.
37 X. Fan, Z. Li and X. J. Loh, *Polym. Chem.*, 2016, **7**, 5898–5919.
38 R. Ye, A. V. Zhukhovitskiy, C. V. Deraedt, F. D. Toste and G. A. Somorjai, *Acc. Chem. Res.*, 2017, **50**, 1894–1901.
39 T. Rudolph, M. von der Lühe, M. Hartlieb, S. Norsic, U. S. Schubert, C. Boisson, F. D'Agosto and F. H. Schacher, *ACS Nano*, 2015, **9**, 10085–10098.
40 S. H. Jo, H. W. Kim, M. Song, N. J. Je, S.-H. Oh, B.-Y. Chang, J. Yoon, J. H. Kim, B. Chung and S. I. Yoo, *ACS Appl. Mater. Interfaces*, 2015, **7**, 18778–18785.
41 F. H. Schacher, P. A. Rupar and I. Manners, *Angew. Chem., Int. Ed.*, 2012, **51**, 7898–7921.
42 E. M. Sulman, V. G. Matveeva, M. G. Sulman, G. N. Demidenko, P. M. Valetsky, B. Stein, T. Mates and L. M. Bronstein, *J. Catal.*, 2009, **262**, 150–158.
43 J. Schöbel, C. Hils, A. Weckwerth, M. Schlenk, C. Bojer, M. C. A. Stuart, J. Breu, S. Förster, A. Greiner, M. Karg and H. Schmalz, *Nanoscale*, 2018, **10**, 18257–18268.
44 J. Schöbel, M. Karg, D. Rosenbach, G. Krauss, A. Greiner and H. Schmalz, *Macromolecules*, 2016, **49**, 2761–2771.
45 C.-L. Zhang and S.-H. Yu, *Chem. Soc. Rev.*, 2014, **43**, 4423–4448.
46 S. Agarwal, A. Greiner and J. H. Wendorff, *Prog. Polym. Sci.*, 2013, **38**, 963–991.
47 C. Bojer, K. Ament, H. Schmalz, J. Breu and T. Lunkenbein, *CrystEngComm*, 2019, **21**, 4840–4850.
48 U. Tritschler, S. Pearce, J. Gwyther, G. R. Whittell and I. Manners, *Macromolecules*, 2017, **50**, 3439–3463.
49 R. L. N. Hailes, A. M. Oliver, J. Gwyther, G. R. Whittell and I. Manners, *Chem. Soc. Rev.*, 2016, **45**, 5358–5407.
50 X. Wang, G. Guerin, H. Wang, Y. Wang, I. Manners and M. A. Winnik, *Science*, 2007, **317**, 644–647.
51 J. B. Gilroy, T. Gädt, G. R. Whittell, L. Chabanne, J. M. Mitchels, R. M. Richardson, M. A. Winnik and I. Manners, *Nat. Chem.*, 2010, **2**, 566–570.
52 P. A. Rupar, L. Chabanne, M. A. Winnik and I. Manners, *Science*, 2012, **337**, 559–562.
53 T. Gädt, N. S. Ieong, G. Cambridge, M. A. Winnik and I. Manners, *Nat. Mater.*, 2009, **8**, 144–150.
54 J. Xu, H. Zhou, Q. Yu, G. Guerin, I. Manners and M. A. Winnik, *Chem. Sci.*, 2019, **10**, 2280–2284.
55 A. M. Oliver, R. J. Spontak and I. Manners, *Polym. Chem.*, 2019, **43**, 3577.
56 Z. M. Hudson, C. E. Boott, M. E. Robinson, P. A. Rupar, M. A. Winnik and I. Manners, *Nat. Chem.*, 2014, **6**, 893–898.
57 H. Qiu, Z. M. Hudson, M. A. Winnik and I. Manners, *Science*, 2015, **347**, 1329–1332.

58 X. Li, Y. Gao, C. E. Boott, M. A. Winnik and I. Manners, *Nat. Commun.*, 2015, **6**, 8127.
59 H. Dou, M. Li, Y. Qiao, R. Harniman, X. Li, C. E. Boott, S. Mann and I. Manners, *Nat. Commun.*, 2017, **8**, 426.
60 J. Schmelz, M. Karg, T. Hellweg and H. Schmalz, *ACS Nano*, 2011, **5**, 9523–9534.
61 B. Fan, L. Liu, J.-H. Li, X.-X. Ke, J.-T. Xu, B.-Y. Du and Z.-Q. Fan, *Soft Matter*, 2016, **12**, 67–76.
62 W. Yu, M. Inam, J. R. Jones, A. P. Dove and R. K. O'Reilly, *Polym. Chem.*, 2017, **8**, 5504–5512.
63 M. Inam, G. Cambridge, A. Pitto-Barry, Z. P. L. Laker, N. R. Wilson, R. T. Mathers, A. P. Dove and R. K. O'Reilly, *Chem. Sci.*, 2017, **8**, 4223–4230.
64 X. Li, P. J. Wolanin, L. R. MacFarlane, R. L. Harniman, J. Qian, O. E. C. Gould, T. G. Dane, J. Rudin, M. J. Cryan, T. Schmaltz, H. Frauenrath, M. A. Winnik, C. F. J. Faul and I. Manners, *Nat. Commun.*, 2017, **8**, 15909.
65 D. Tao, C. Feng, Y. Cui, X. Yang, I. Manners, M. A. Winnik and X. Huang, *J. Am. Chem. Soc.*, 2017, **139**, 7136–7139.
66 J. R. Finnegan, X. He, S. T. G. Street, J. D. Garcia-Hernandez, D. W. Hayward, R. L. Harniman, R. M. Richardson, G. R. Whittell and I. Manners, *J. Am. Chem. Soc.*, 2018, **140**, 17127–17140.
67 M. C. Arno, M. Inam, Z. Coe, G. Cambridge, L. J. Macdougall, R. Keogh, A. P. Dove and R. K. O'Reilly, *J. Am. Chem. Soc.*, 2017, **139**, 16980–16985.
68 J. Schöbel, M. Burgard, C. Hils, R. Dersch, M. Dulle, K. Volk, M. Karg, A. Greiner and H. Schmalz, *Angew. Chem., Int. Ed.*, 2017, **56**, 405–408.
69 A. Greiner and J. H. Wendorff, *Angew. Chem., Int. Ed.*, 2007, **46**, 5670–5703.
70 F. Mitschang, H. Schmalz, S. Agarwal and A. Greiner, *Angew. Chem., Int. Ed.*, 2014, **53**, 4972–4975.
71 P. A. Schaal and U. Simon, *Beilstein J. Nanotechnol.*, 2013, **4**, 336–344.
72 W. S. Rasband, *ImageJ*, U. S. National Institutes of Health, Bethesda, Maryland, USA, 1997–2018.
73 P. Raffa, C. Evangelisti, G. Vitulli and P. Salvadori, *Tetrahedron Lett.*, 2008, **49**, 3221–3224.
74 T. Taguchi, K. Isozaki and K. Miki, *Adv. Mater.*, 2012, **24**, 6462–6467.
75 T. Mitsudome, Y. Yamamoto, A. Noujima, T. Mizugaki, K. Jitsukawa and K. Kaneda, *Chem.–Eur. J.*, 2013, **19**, 14398–14402.